Numerical Simulation of Incompressible Two-Blade Rotor Flowfields

John A. Ekaterinaris*

Risoe National Laboratory, 4000 Roskilde, Denmark

The incompressible flowfield of a two-blade rotor with untapered, untwisted, aspect-ratio-six blades is computed. The artificial compressibility formulation of the incompressible-flow equations is chosen for the numerical solution. Time integration is performed implicitly and space discretization is obtained with an upwind-biased scheme. The numerical method is implemented on a multiblock solver where turbulent flow can be computed by both algebraic and one-equation models. The flowfield is computed on a half-rotor configuration by imposing periodicity conditions in the azimuthal direction. The numerical mesh over the blade consists of three distinct blocks and is wrapped on a cylindrical surface. Turbulence is modeled with a one-equation turbulence model. Comparisons of the computed results with available experimental data are presented.

Nomenclature

$A^\pm$	=	flux Jacobian matrix
$\tilde{F}, \tilde{G}, \tilde{H}$	=	numerical fluxes
$\hat{f}, \hat{g}, \hat{h}$	=	flux vectors
p	=	pressure
$\hat{Q}$	=	primitive variables vector
U, V, W	=	contravariant velocity components
u, v, w	=	Cartesian velocity components
X, X^{-1}	=	eigenvector matrices
x, y, z	=	Cartesian coordinates
β	=	pseudocompressibility parameter
$\Delta F^\pm$	=	flux difference
Λ	=	eigenvalue matrix
ξ, η, ζ	=	curvilinear coordinates
ω	=	rotational velocity

I. Introduction

THE exploitation of wind energy is not a new concept. In recent years, however, higher fuel costs and technological advances in wind-turbine design along with ecological considerations have made the utilization of wind turbines increasingly more widespread. The aerodynamics of wind turbines share certain common characteristics with the aerodynamics of helicopter rotors in hover. Progress in helicopter rotor aerodynamics, which remains a subject of continuous interest, can support and assist ongoing wind-turbine investigations. Both wind turbines and hovering helicopter rotor blades operate in a rotating flow environment. In addition, wind-turbine blades are subject to unsteady aerodynamic forces analogous to loading caused by dynamic stall on helicopter blades in forward flight, when the wind turbine operates in yaw and nonuniform freestream conditions. Apart from these similarities, wind turbines and helicopter–rotor blade aerodynamics have certain differences. For example, compressibility is important for helicopter rotors because the rotational speed is high, whereas wind-turbine flows are incompressible. Most wind turbines are

stall-regulated and have tapered, highly twisted blades. The airfoil sections are cambered and thick. As a result, the flow of the wind-turbine blades exhibits more separation compared to hovering helicopter rotor blades that also operate at lower angles of incidence. The wind-turbine efficiency is also greatly affected by the wind conditions.

It is recognized that the rotating-flow environment is one of the first-order factors affecting the flowfield development over wind-turbine blades. Rotational flow effects for helicopter rotors in hover were investigated previously both experimentally[1] and numerically.[2-7] Numerical simulations of helicopter rotor flows were obtained either by using a prescribed wake geometry with potential, Euler and Navier–Stokes flow solvers,[5] or by direct wake-capturing methods.[2] The specified wake geometry depends, however, on the particular blade shape. Capturing of the full-wake dynamics, on the other hand, of both helicopter and wind-turbine rotors, is a challenge for current computational fluid dynamics (CFD) methods. Numerical studies[7] have shown that to enable full capturing of the helical wake it is required to use high-order accurate numerical methods, sufficient grid resolution in the vortex core, and a grid-adaptive scheme.

The goal of this study is to develop a numerical tool for the prediction and investigation of realistic wind-turbine rotor flowfields. A method capable of treating blades with arbitrary shape, twist, taper, and airfoil section is needed. Therefore, the choice was made to simulate the entire flowfield of a lifting rotor including the wake and its induced effects using an approach similar to the method presented in Ref. 2. Wind turbines operate at lower rotation speeds compared to helicopter rotors and have helical wakes with larger pitch. As a result, numerical solutions without grid-adaptive capabilities will require an enormous number of grid points to capture many revolutions of the helical wake. It is expected, however, that only the near wake will have significant effect. Therefore, accurate predictions of the wind-turbine blade surface loads and performance can be achieved with CFD solutions. To date, wind-turbine flow investigations have not taken a full account of the rotational effects on the flowfield development. In Ref. 8, for example, the incompressible flowfield of a single rotating wind-turbine blade was investigated numerically.

The scope of this investigation is to demonstrate the ability of an incompressible-flow solver, based on the artificial compressibility formulation, to compute incompressible flows over rotating blades. The rotational-flow effects may be taken into account either by rotating the grid or by incorporating the rotational blade velocities in the governing equations as fictitious

*Senior Research Scientist, Test Station for Wind Turbines, Wind Energy and Meteorology Department; currently Senior Research Scientist, Nielsen Engineering and Research, Inc., Mountain View, CA 94043. Associate Fellow AIAA.

forces. Numerical simulation of a wind turbine including the tower and the nacelle will require the rotation of the blades. In this investigation, a method for the computation of incompressible flows over rotors is presented and the numerical results are validated for a single two-blade rotor without blade/tower interference effects. The flow solver can account for rotational flow effects by both adding fictitious forces and by grid rotation. The solution is initialized on a stationary grid where the rotational effects are incorporated through fictitious body forces. The final solution of the two-blade rotor flowfield, however, is obtained from a time-accurate solution by rotating the grid. The high Reynolds number turbulent flow can be modeled with the algebraic Baldwin and Lomax[9] eddy-viscosity turbulence model and the one-equation Spalart and Allmaras[10] and Baldwin and Barth[11] turbulence models. In this paper, the Spalart and Allmaras, one-equation turbulence model is used to compute turbulent flows. The numerical procedure is validated with the available experimental measurements of Ref. 1.

A computational mesh for the half-rotor configuration is used. Periodicity conditions are imposed in the azimuthal direction. The entire grid consists of three distinct blocks. The main grid block includes the blade surface, the near-field viscous region, and the trailing-edge and tip wakes. Two additional blocks are used to extend the domain to the far field. In the following sections, the grid generation procedure is described in detail. The numerical method and the boundary conditions used for the numerical solution are presented. The computed results and comparisons with available experiments are shown.

II.   Governing Equations

The incompressible-flow equations for a curvilinear coordinates system ξ, η, and ζ are

$$\nabla \cdot \hat{U} = \frac{\partial}{\partial \xi}\left(\frac{U}{J}\right) + \frac{\partial}{\partial \eta}\left(\frac{V}{J}\right) + \frac{\partial}{\partial \zeta}\left(\frac{W}{J}\right) = 0 \qquad (1)$$

$$\frac{\partial \hat{u}}{\partial t} + \frac{\partial \hat{f}}{\partial \xi} + \frac{\partial \hat{g}}{\partial \eta} + \frac{\partial \hat{h}}{\partial \zeta} = \frac{1}{Re}(\hat{f}_v + \hat{g}_v + \hat{h}_v) \qquad (2)$$

here, J is the Jacobian of the coordinate transformation, $\hat{U} = (U, V, W)/J$, $\hat{u} = (u, v, w)/J$, and $\hat{f}$, $\hat{g}$, and $\hat{h}$ are the inviscid flux vectors given in Refs. 19 and 20.

In Eqs. (1) and (2), u, v, and w are the Cartesian velocity components and U, V, and W are the contravariant velocity components along ξ, η, and ζ directions, respectively. The contravariant V velocity along ξ, for example, is $U = \xi_x u + \xi_y v + \xi_z w$.

The primary problem with numerical solutions of the incompressible-flow equations is the difficulty of coupling changes in the velocity field with changes in the pressure field while satisfying the continuity equation. The incompressible-flow equations include pressure in a non-time-dependent form because the continuity equations have a nonevolutionary character. The non-time-dependent form of pressure is the source of difficulties of numerical schemes that must treat continuity with special techniques. The alternative stream function/vorticity and vorticity/velocity[12] formulations of the incompressible-flow equations do not present the same difficulties with the primitive variable formulation, but their application is only straightforward for two-dimensional flows. Numerical solutions of primitive variable formulations are obtained either with the Poisson equation for pressure method[13,14] or with fractional time-step methods.[15,16]

The pressure Poisson method utilizes a Poisson equation in pressure, which is obtained from the momentum equations. It advances the velocity field in time using the momentum equations and subsequently solves the Poisson equation for the pressure at the current time level so that continuity is satisfied

at the next time level. The pressure Poisson method couples, therefore, velocity and pressure indirectly. The fractional time-step method, introduced by Chorin,[15] first solves for an intermediate velocity field from the momentum equations and then obtains the pressure field that will map the intermediate velocity into a divergent-free velocity.

The artificial compressibility or pseudocompressibility method can be used as an alternative to the preceding two methods. This method was initially introduced by Chorin[17] for the solution of steady-state incompressible flows. The artificial compressibility formulation for steady-state solutions is obtained by adding a pseudotime derivative of pressure to the continuity equation. The pressure-time derivative term directly couples the pressure with velocity and allows time marching the equations until a divergence-free velocity field is obtained. The pseudocompressibility method has been extended for the solution of unsteady flows.[18] Time-accurate numerical solutions of incompressible, high Reynolds number, turbulent, two-[19] and three-dimensional[20] flows were obtained using the unsteady formulation of the pseudocompressibility method. The artificial compressibility method is presented for the transformed form of the governing equations.

The artificial compressibility formulation is obtained from the original incompressible-flow equations by introducing an additional time derivative of pressure to the continuity equation as follows:

$$\frac{\partial p}{\partial \tau} = -\beta \nabla \cdot \hat{U} \qquad (3)$$

Addition of this fictitious pressure derivative enables full coupling of continuity with the momentum equations. The artificial compressibility form of the incompressible-flow governing equations is very similar to the compressible-flow equations. As a result, techniques developed for numerical solutions of the compressible-flow equations can be applied to the numerical solution of incompressible flows with the pseudocompressibility method. In Eq. (3) τ does not represent physical time, and when t in the momentum equations is replaced by τ, the pseudocompressible form of the governing equations is

$$\frac{\partial \hat{Q}}{\partial \tau} + \frac{\partial \hat{F}}{\partial \xi} + \frac{\partial \hat{G}}{\partial \eta} + \frac{\partial \hat{H}}{\partial \zeta} = \frac{1}{Re}(\hat{F}_v + \hat{G}_v + \hat{H}_v) \qquad (4)$$

where $\hat{Q} = [p, u, v, w]^T/J$ is the solution variable vector and $\hat{F}$, $\hat{G}$, and $\hat{H}$ are the inviscid fluxes with

$$\hat{F} = \frac{1}{J}\begin{bmatrix} \beta U \\ uU + \xi_x p + \xi_t u \\ vU + \xi_y p + \xi_t v \\ wU + \xi_z p + \xi_t w \end{bmatrix}$$

and similar forms for $\hat{G}$ and $\hat{H}$ and the viscous terms are

$$\hat{F}_v = \frac{1}{J}\begin{bmatrix} 0 \\ (\nabla \xi \cdot \nabla \xi)u_\xi + (\nabla \xi \cdot \nabla \eta)u_\eta + (\nabla \xi \cdot \nabla \zeta)u_\zeta \\ (\nabla \eta \cdot \nabla \xi)u_\xi + (\nabla \eta \cdot \nabla \eta)u_\eta + (\nabla \eta \cdot \nabla \zeta)u_\zeta \\ (\nabla \zeta \cdot \nabla \xi)u_\xi + (\nabla \zeta \cdot \nabla \eta)u_\eta + (\nabla \zeta \cdot \nabla \zeta)u_\zeta \end{bmatrix}$$

and similarly for the $\hat{G}_v$ and $\hat{H}_v$ terms.

In these equations τ is referred to as pseudotime, which can be considered as a time-iteration parameter. Steady-state incompressible solutions are obtained with the artificial compressibility method by time marching as in the compressible case. The numerical methods for steady-state solutions of the pseudocompressible equations are very similar to time-marching methods used for the solutions of the compressible flow equations. At convergence, however, the time derivative of pressure and, consequently, the divergence of the velocity approaches zero. The parameter β usually has a value between

1 and 5, but larger values may be required for solutions on highly stretched grids. The value of $\boldsymbol{\beta}$ in these cases is adjusted accordingly so that optimal convergence is obtained.

The computation of the flowfield of the rotor can be performed either by a steady-state solution on a stationary grid and noninertial rotating reference frame or by a time-accurate solution on a rotating grid. When the grid rotates, the centrifugal and Coriolis force effects are obtained through the unsteady metric terms ξ_t, η_t, and ζ_t, which are included in the governing equations. For a stationary grid, rotational flow effects are introduced by adding body forces to the governing equations. The total body force per unit volume $\boldsymbol{F}_b$ is the sum of the centrifugal $\boldsymbol{F}_c$ and Coriolis $\boldsymbol{F}_{Cor}$ forces. This force is given by

$$\boldsymbol{F}_b = \boldsymbol{F}_c + \boldsymbol{F}_{Cor} = (\omega \times r) \times \omega - 2\omega \times V \qquad (5)$$

where r is the position vector and $V = (u, v, w)^T$ is the velocity vector. For a frame rotating around the z axis, $\omega = (0, 0, \omega_z)^T$, and the total force per unit volume is

$$\boldsymbol{F}_b = \begin{bmatrix} 0 \\ \omega_z^2 x + 2\omega_z v \\ \omega_z^2 y - 2\omega_z u \\ 0 \end{bmatrix} \qquad (6)$$

When this force is added to the right-hand side (RHS) of the governing equations, then the solution of the rotor flowfield can be obtained on a stationary grid. In this paper, the solution is obtained by rotating the grid because the objective of this study is to develop a method suitable for the computation of general, three-dimensional, unsteady flowfields of wind turbines capable of capturing interference effects between moving and stationary components, such as the rotating blade and the wind-turbine tower. To accelerate convergence and reduce the total computing time, the solution on a noninertial reference frame is used as the initial condition for the unsteady solution with a rotating grid.

III. Numerical Implementation

Half-rotor configuration solutions are computed and periodicity conditions are imposed on the symmetry plane computational boundaries. The topology of the numerical grid that is used for the computations is described first. The implicit, time-accurate integration scheme and the space discretization method are presented next. Finally, the boundary conditions used for the computation of the rotor flowfield are given.

A. Numerical Mesh

The blade surface grid and the coordinate system definitions are shown in Fig. 1. The blade sections are represented by a
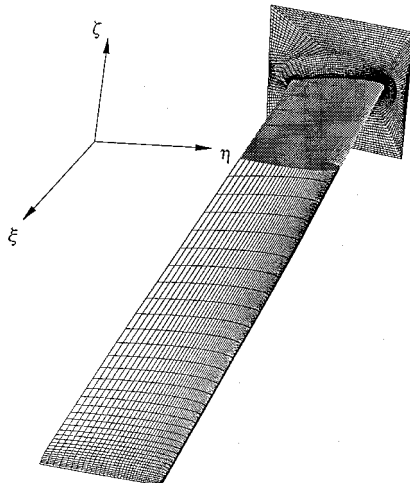
sequence of O-type grids. The flowfield of the two-blade rotor in hover is symmetric in the azimuthal η direction. Therefore, a numerical mesh for only one blade is constructed and periodicity is imposed in the azimuthal direction. The entire grid has a topology of a half cylinder with its symmetry axis aligned along the z or ζ coordinate direction. The grid surfaces at the symmetry plane ($\phi = 0$, π, Fig. 2) are by construction planes with identical grid-point distribution, so that periodicity boundary conditions in the azimuthal η direction are applied. The periodic boundaries are located at $\phi = 0$ and $\phi = \pi$. The viscous region near the blade surface, the trailing edge, and tip wakes are represented by this single-block, O–H-type grid. Two more grid blocks are used to extend the grid in the ζ direction to facilitate treatment of the inflow/outflow boundary conditions.

The numerical grid, which is shown in Fig. 2 in perspective view, is constructed as follows. First an O–H-type mesh is made for a straight blade (Fig. 1) and the wake region beyond the blade tip. The outer boundary of this mesh in the spanwise direction extends one body radius away from the blade tip. The grid surfaces in each spanwise station are O-type grids for each blade section. The outer boundary of these O-type grids has a rectangular shape, where the vertical edges have the same number and identical distribution of grid points. The length of the horizontal side of each spanwise location plane grid surface is approximately equal to half the periphery of a circle centered at the blade rotation center. This mesh is subsequently mapped on a half-cylinder surface. The left and right vertical faces become the periodic boundaries. A typical deformed O-type grid surface is shown in Fig. 3.

After mapping, the top and bottom faces (Fig. 2) deform to conical surfaces. Two more blocks are added to the top and bottom conically-shaped main grid faces to extend the domain to the far field and facilitate the implementation of boundary conditions. A large grid extent is required on the pressure side of the blade, below the rotor blade, to convect the helical wing-
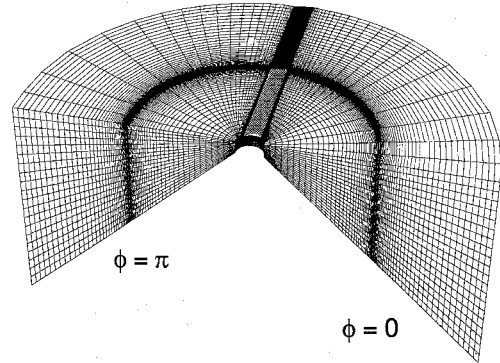

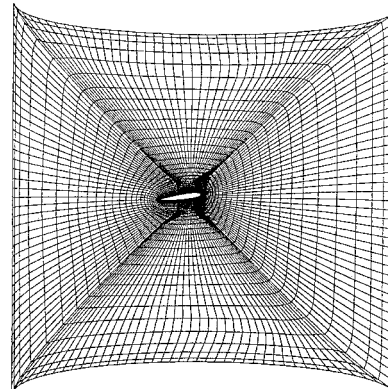Fig. 2   Perspective view of bottom-half part of the blade grid.

Fig. 3   Typical O-type grid surface of cross section along the blade span.

Fig. 1   Blade surface grid.

tip vortex. The grid on the top must also be extended far enough to the far field so that the velocities induced by the presence of the rotor are small. The upper and lower blocks are simple extensions of the top and bottom conical surfaces and they are not shown in Fig. 2. These blocks extend to 10 rotor radii away from the blade surface.

The blade angle of incidence can be taken into account either by adding a constant plunge velocity along the rotational axis or by setting the blade at an incidence. To simplify the numerical implementation the blade is rotated to a specified angle with respect to the horizontal before the grid is mapped on a cylindrical surface. The blade incidence can be seen in Figs. 1 and 3 before and after mapping, respectively.

B. Time Integration

The three-dimensional Navier–Stokes equations in the artificial compressibility formulations are integrated using implicit time integration. Steady-state solutions of Eq. (4) do not require time accuracy. Therefore, the pseudotime derivative is discretized by a first-order-accurate formula as follows:

$$\left[\frac{I}{\Delta\tau} + \left(\frac{\partial R}{\partial Q}\right)^m\right]\Delta Q = -R^m \tag{7}$$

where R is the RHS residual term given by $R = (\hat{F} - \hat{F}_v)_{\xi} + (\hat{G} - \hat{G}_v)_{\eta} + (\hat{H} - \hat{H}_v)_{\zeta}$ and $\Delta Q = Q^{m+1} - Q^m$. Equation (7) is marched implicitly in time until convergence is obtained using the Gauss–Seidel line-relaxation method. This method was originally proposed by Chakravarthy[21] and MacCormack[22] and subsequently implemented for incompressible-flow solutions with the artificial compressibility method for Rogers et al.[19,20] The rotating blade flowfield can be computed by a steady-state solution on a noninertial, reference frame that includes the fictitious body force terms. The noninertial reference frame fictitious forces are treated implicitly by adding the term $\partial F_b/\partial Q$ to the left-hand side operator of Eq. (7). This term is given by

$$\frac{\partial F_b}{\partial Q} = \begin{bmatrix} 0 & 0 & 0 & 0 \\ 0 & 0 & 2\omega_z & 0 \\ 0 & -2\omega_z & 0 & 0 \\ 0 & 0 & 0 & 0 \end{bmatrix} \tag{8}$$

For time-accurate solutions the time derivatives of the velocity vector u in the momentum equations are obtained from the following backward, second-order, three-time level formula as $(1.5u^{n+1} - 2u^n + 0.5u^{n-1})/\Delta t = -R^{n+1}$. The momentum equations are solved for a divergence-free velocity field at the $n+1$ time level by introducing a pseudotime level that is denoted by the superscript m in the following artificial compressibility relation:

$$\frac{\partial p}{\partial \tau} = -\boldsymbol{\beta}\nabla\cdot u^{n+1,m+1} \tag{9}$$

Iterative solution of this equation is performed so that $u^{n+1,m+1}$ approaches u^{n+1} as the divergence $\nabla\cdot u^{n+1,m+1}$ approaches zero.

The delta form of the linearized solution algorithm, for both steady-state and time-accurate solutions, is given by

$$\left[\frac{I_t}{J} + \left(\frac{\partial R}{\partial Q}\right)^{n+1,m}\right]\times(Q^{n+1,m+1} - Q^{n+1,m}) = -R^{n+1,m}$$

$$- \frac{I_m}{\Delta t}(1.5Q^{n+1,m} - 2Q^n + 0.5Q^{n-1}) \tag{10}$$

where $I_t = \text{diag}[\Delta t/\Delta\tau, 1.5, 1.5, 1.5]/\Delta t$ and $I_m = \text{diag}[0, 1, 1, 1, 1]$. The algorithm for steady-state solutions is obtained from

Eq. (10) when the internal iteration index m is dropped and only the term R is retained on the RHS.

C. Space Discretization

Addition of the pressure-time derivative in the continuity equation introduces artificial waves. Therefore, the space discretization method must be able to follow and properly propagate these artificial waves through the computational domain. In addition, these waves must be carried out of the computational domain using appropriate boundary conditions. Space discretization must be performed with a scheme that provides some dissipative mechanism that automatically suppresses the oscillations caused by the nonlinear convective fluxes. Central difference space discretization requires additional artificial dissipation[23] to avoid odd–even coupling caused by the nonlinear inviscid terms. Upwind space differencing, on the other hand, follows the waves introduced by artificial compressibility and inherently has a dissipative mechanism that automatically suppresses oscillations. In the present work, Roe[24] upwind flux differencing is used because it is independent of externally specified parameters, as opposed to central difference schemes with added artificial dissipation. Even though upwind schemes require, in general, more computation time per time step, they converge faster. As a result, savings in the overall computing time are obtained.

Roe's flux-difference splitting[24] approximates the convective flux derivative by

$$\frac{\partial\hat{F}}{\partial\xi} \approx \frac{F_{i+1/2} - F_{i-1/2}}{\Delta\xi} \tag{11}$$

where $\tilde{F}_{i+1/2}$ is a numerical flux given by

$$\tilde{F}_{i+1/2} = \tfrac{1}{2}[\hat{F}(Q_{i+1}) + \hat{F}(Q_i)] - f_{i+1/2} \tag{12}$$

In this equation the first two terms yield the second-order, central-difference scheme and the term $f_{i+1/2}$ represents an upwinding dissipative term depending on the flux difference of the positive and negative traveling waves. First-order upwinding is obtained when $f_{i+1/2} = \Delta F_{i+1/2}^+ - \Delta F_{i+1/2}^-$.

In practice, a first-order scheme is too diffusive to allow solutions with a reasonable number of grid points. Therefore, the following third- and fifth-order upwind-biased formulas are used. For the third-order, upwind-biased scheme, the term $f_{i+1/2}$ is computed as

$$f_{i+1/2} = -\tfrac{1}{3}[\Delta F_{i-1/2}^+ - \Delta F_{i+1/2}^+ + \Delta F_{i+1/2}^- - \Delta F_{i+3/2}^-] \tag{13}$$

and the fifth-order scheme is obtained for

$$f_{i+1/2} = -\tfrac{1}{30}(-2\Delta F_{i-3/2}^+ + 11\Delta F_{i-1/2}^+ - 6\Delta F_{i+1/2}^+ - 3\Delta F_{i+3/2}^+$$

$$+ 2\Delta F_{i+5/2}^- - 11\Delta F_{i+3/2}^- + 6\Delta F_{i+1/2}^- + 3\Delta F_{i-1/2}^-) \tag{14}$$

In these equations the flux difference is computed as $\Delta F_{i+1/2}^{\pm} = A^{\pm}(\bar{Q})\times(Q_{i+1} - Q_i)$, where $\bar{Q}$ is the vector of Roe average variables, which for incompressible flow becomes $\bar{Q} = (Q_{i+1} + Q_i)/2$. A^+, A^- are the parts of the flux Jacobian matrix $A = \partial\hat{F}/\partial\hat{Q}$ with only positive and only negative eigenvalues, respectively, given by $A^{\pm} = X\Lambda^{\pm}X^{-1}$, and X and X^{-1} are the right and left eigenvectors of the flux Jacobian matrix A, and $\Lambda^{\pm}$ is a diagonal matrix containing both positive and negative eigenvalues on the main diagonal.

D. Boundary Conditions

On the blade surface the viscous nonslip condition is enforced for the velocities, and the pressure is extrapolated from the interior solution. In the computations, the blade tip is modeled like a wedge and the grid lines collapse after the tip to form a singular plane. For this part of the grid, the flow variables are averaged from the lower and upper parts of the grid.

At the inner cylindrical surface, the flow variables are obtained by assuming a hub where a slip boundary condition is applied. The grid resolution along the ξ coordinate direction is too coarse to apply a viscous nonslip condition usually encountered on a wind-turbine nacelle. The velocities are obtained from the interior solution by assuming tangential flow on the inner, cylindrical grid surface, and the pressure is obtained from the interior by assuming zero pressure gradient in the spanwise or ξ direction.

A periodicity condition is applied in the blade azimuthal direction. This boundary condition swaps the flow information at the symmetry plane boundaries of the grid. These boundaries are located at $\phi = 0$ and $\phi = \pi$ (Fig. 2), and because they are identical planes, no interpolation is needed for transferring the flow variables. The boundary above the rotor plane is an inflow. The other far-field boundaries in the radial direction, which are cylindrical surfaces, are updated explicitly assuming a no-flow condition. Imposing a no-flow condition at these far-field boundaries produces a closed box for the rotor flowfield that resembles the conditions of the experiment and causes the flow to recirculate in the computational domain. Part of the computational boundary located at the far field below the rotor plane is treated as an outflow, where the flow velocity is obtained from momentum theory concepts as in Refs. 7 and 25. It is assumed that the flow exists through a circular hole of half the rotor disc area with an outflow velocity magnitude twice the average value of the velocity the momentum theory determines for the plane through the rotor. The outflow boundary is located far enough from the blade so that simple characteristic-type outflow boundary conditions are imposed.

IV. Results

The numerical method presented in the last section is tested for the computation of a model rotor flowfield. The rotor flowfield was studied experimentally in Ref. 1. The experiments of Ref. 1 were focused on the investigation of flowfields at transonic-tip Mach numbers, which are of more interest to helicopter flows. The rotor blades are untwisted, and all of the cross sections are identical NACA 0012 airfoils. The blade aspect ratio is six chord lengths. Results for low tip speed, M_t = 0.22, exist for α = 5 and 8 deg. For M_t = 0.22, the rotational speed is ω_z = 650 rpm and the experimental Reynolds number is $Re_c \approx 0.98 \times 10^6$. In the computations the flowfield is assumed to be fully turbulent and the solution is obtained for $Re_c = 1.0 \times 10^6$ with the Spalart–Allmaras one-equation turbulence model. For low angle of incidence, it is expected that the flow is attached. For these conditions, the Baldwin–Lomax algebraic eddy–viscosity model is expected to yield sufficient accuracy. However, in wind-turbine flows the flow is highly separated and the one-equation models will be required.

A fine grid that has approximately 10^6 points and a coarse grid with 30% fewer points were used. Both grids have the same topology described in Sec. III.A. The blade and the wake region in the fine grid are computed with an $81 \times 161 \times 61$-point grid along the spanwise, chordwise, and normal, or ξ, η, and ζ directions, respectively. The other two blocks, which are used to extend to the far field, are $81 \times 41 \times 41$ Cartesian-type grids. For the coarse grid, the blade is represented by a $61 \times 141 \times 61$-point grid and the far-field blocks are $61 \times 35 \times 41$-point grids. There is one point overlap between these grids and the main blade grid. At these boundaries, zonal boundary conditions are imposed. All grids are rotated at each time step by the same angle $\Delta\phi$. The rotation angle depends on the time step used for the unsteady calculation. Grid rotation at constant angular velocity ω_z induces rotational speeds $u_g = dx/dt = -\omega_z y$ and $u_g = dy/dt = \omega_z x$. The unsteady metrics for this motion are $\xi_t = u_g \xi_x + v_g \xi_y$, $\eta_t = u_g \eta_x + v_g \eta_y$, and $\zeta_t = 0$.

All lengths are normalized with the blade chord length. The velocities are nondimensionalized with the wingtip speed V_t,

which is equal to one in the computations. The nondimensional rotation speed is $\hat{\omega} = V_t/R$. The period for one rotation $T = 2\pi/\hat{\omega}$ is computed in 1000 time steps that correspond to a nondimensional time step $\Delta t \approx 0.035$. The solution is initialized on a stationary grid with the noninertial frame fictitious force terms to obtain an initial pressure field distribution. Then, the unsteady solution on the rotating grid is computed. After approximately 500 iterations the solution converges and no difference on the computed surface pressures is observed.

Computed solutions for the α = 5 and 8 deg collective angle of incidence are compared with the available surface pressure measurements of Ref. 1. The computed surface pressure coefficient distributions at half-span location, $r/R = 0.5$ obtained from the fine and coarse grid solutions, are compared with the measurements of Ref. 1 in Fig. 4. There is good agreement with the experiment for both solutions. Further comparisons with the experiment for $r/R = 0.68$, 0.8, and 0.89 are shown in Figs. 5, 6, and 7, respectively. For this small collective angle of incidence, there is little difference between the coarse and fine grid solutions in the tip region. Comparisons of the α = 8 deg solution with the experiment at the same spanwise locations are shown in Figs. 8–11. The largest differences between the fine and coarser grid solutions are obtained again at the tip region. For all spanwise locations both computations closely match the measured values of the surface pressure coefficient. For wind-turbine flowfields the collective angle of incidence is much larger and the flow over the blade usually includes large regions of separated flow, particularly for spanwise locations closer to the rotation axis. Wind-turbine computations will require larger-size grids to include the tower, and more computing time will be needed to compute the fully
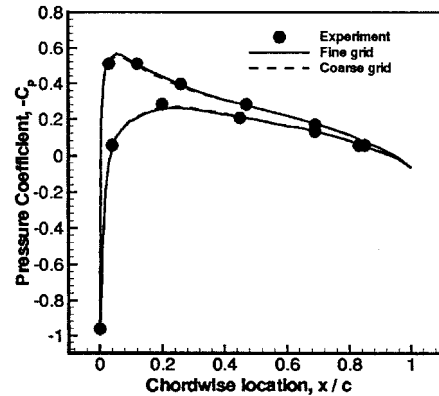

Fig. 4 Comparison of the computed and measured surface pressure coefficient distribution for α = 5 deg and the r/R = 0.50 span location.
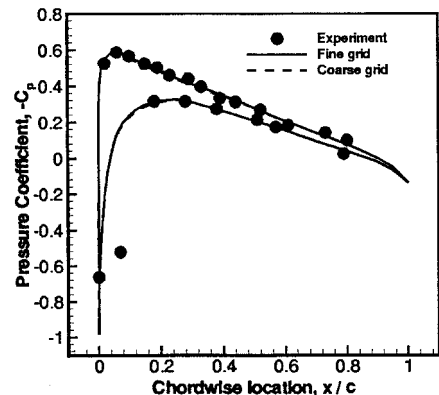

Fig. 5 Comparison of the computed and measured surface pressure coefficient distribution for α = 5 deg and the r/R = 0.68 span location.
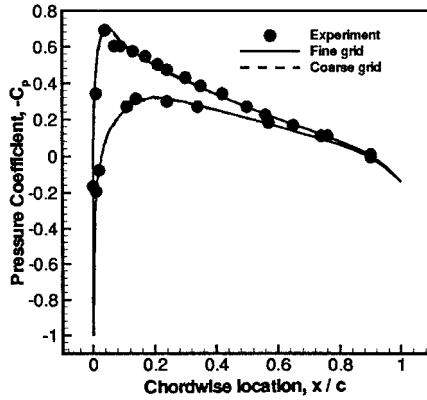
Fig. 6   Comparison of the computed and measured surface pressure coefficient distribution for α = 5 deg and the r/R = 0.80 span location.
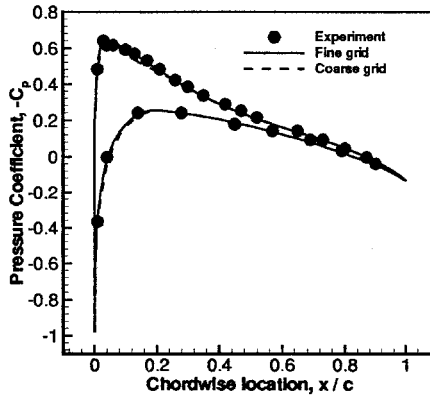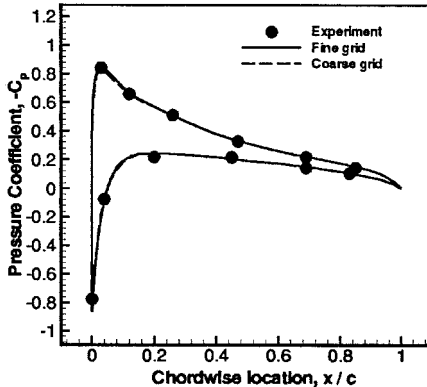

Fig. 7   Comparison of the computed and measured surface pressure coefficient distribution for α = 5 deg and the r/R = 0.89 span location.

Fig. 8   Comparison of the computed and measured surface pressure coefficient distribution for α = 8 deg and the r/R = 0.50 span location.

Fig. 9   Comparison of the computed and measured surface pressure coefficient distribution for α = 8 deg and the r/R = 0.68 span location.

Fig. 10   Comparison of the computed and measured surface pressure coefficient distribution for α = 8 deg and the r/R = 0.80 span location.

Fig. 11   Comparison of the computed and measured surface pressure coefficient distribution for α = 8 deg and the r/R = 0.89 span location.

unsteady flowfield resulting from the rotating blade/tower interaction.

The computed lift coefficient distributions along the span at α = 5 and 8 deg are compared with the measurements in Figs. 12 and 13, respectively. For both cases there is fair agreement with the experiment. Another important parameter for rotor operation is the thrust. Rotor flows include many flow patterns. The wind-turbine or windmill stage is reached when the flow through the rotor disc is retarded, the momentum of the relative flow through the disc is reduced, the trust is reversed, and energy is absorbed from the airstream. Therefore, evaluation of the thrust is important to wind-turbine applications. The numerical procedure is validated by comparing the numerical
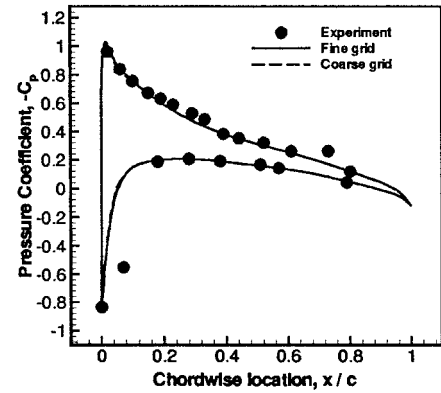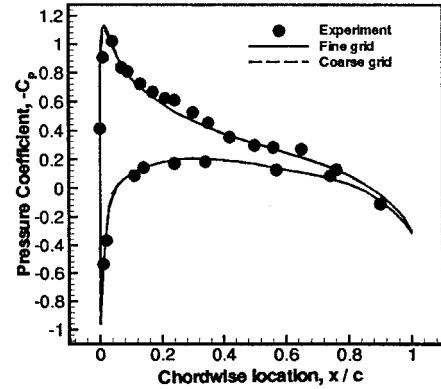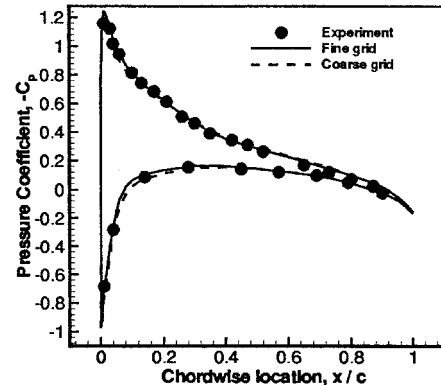
solution with that of a hovering rotor experiment. For this case the computed thrust is 0.002 for collective pitch angle α = 5 deg and 0.004 for α = 8 deg in agreement with the experimental values.

Determination of the helical tip vortex path is important in rotor aerodynamics. For helicopter rotors, where the tip vortex location and strength determine the occurrence and intensity of blade vortex interaction, development of numerical methods capable of predicting accurately the tip vortex is a subject of ongoing investigations. The motivation of this study is to develop a method for numerical predictions of wind-turbine rotational flowfields. The high-order schemes usd for the evaluation of the inviscid fluxes are expected to reduce diffusion of the tip vortex when it convects in the rotor wake. However,
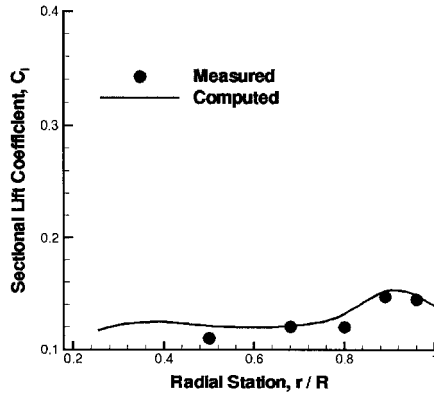
Fig. 12 Comparison of the computed and measured spanwise lift distribution for collective pitch α = 5 deg.
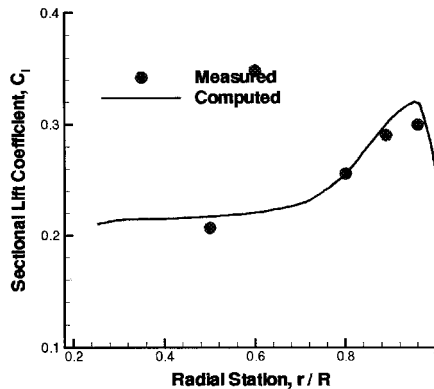

Fig. 13 Comparison of the computed and measured spanwise lift distribution for collective pitch α = 8 deg.
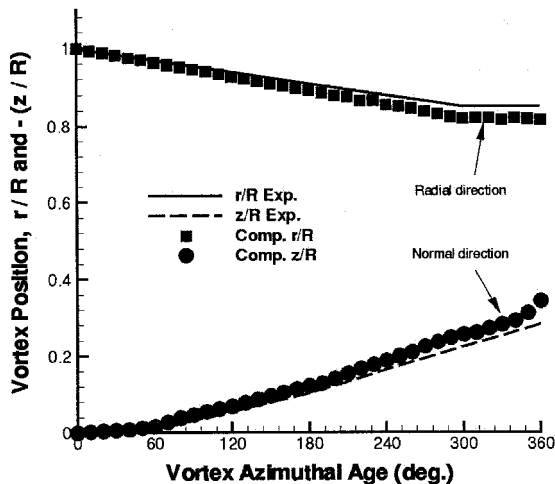

Fig. 14 Comparison of the computed and measured vortex center location in the axial (z) and radial (r) directions for collective pitch α = 8 deg.

full capturing of the tip vortex dynamics requires sufficient grid resolution in the vortex core and a grid adaptive method. In the simulations, the blade geometry at the tip is modeled approximately by a wedge because the objective is to validate the method. A comparison of the vortex location with the measurements is shown in Fig. 14. The predicted vortex location is in general agreement with the measurements.

V. Summary

The artificial compressibility method is used for the numerical solution of the three-dimensional, unsteady, incompressi-

ble-flow equations. Time-accurate solutions are obtained with an implicit, time-marching, line-relaxation procedure. Space discretization is performed with an upwind-biased, high-order accurate scheme. Turbulent flow is modeled with a one-equation turbulence model. The flow solver is tested for the computation of the flowfield of a model two-blade rotor in hover. A half-rotor grid is constructed and periodicity conditions are imposed at the end symmetry planes of the numerical mesh. The solution of the flowfield is obtained by rotating the grid until steady state is achieved. The computed solutions are in agreement with available surface pressure measurements of low-speed flow of the rotor in hover. The present method can be applied to the solution of more complex wind-turbine flows and has the potential to provide predictions of the unsteady flowfield of a blade passing by the tower.

References

[1]Caradonna, F. X., and Tung, C., "Experimental and Analytical Studies of a Model Helicopter Rotor in Hover," NASA TM 81232, Sept. 1981.

[2]Srinivasan, G. R., Beader, J. D., Obahyasi, S., and McCroskey, W. J., "Flowfield of a Lifting Rotor in Hover: A Navier-Stokes Simulation," *AIAA Journal*, Vol. 30, No. 10, 1992, pp. 2371–2378.

[3]Srinivasan, G. R., and McCroskey, W. J., "Navier-Stokes Calculations of Hovering Rotor Flowfields," *Journal of Aircraft*, Vol. 25, No. 10, 1988, pp. 865–874.

[4]Agrawal, R. K., and Deese, J. E., "Euler Calculations of the Flowfield of a Helicopter Rotor in Hover," *Journal of Aircraft*, Vol. 24, No. 4, 1987, pp. 231–238.

[5]Sankar, N. L., Wake, B. E., and Lekoudis, S. G., "Solutions of the Unsteady Euler Equations for Fixed and Rotor Wing Configurations," *Journal of Aircraft*, Vol. 23, No. 3, 1986, pp. 283–289.

[6]Chen, C.-L., and McCroskey, W. J., "Numerical Simulations of Helicopter Multi-Bladed Rotor Flow," AIAA Paper 88-0046, Jan. 1988.

[7]Strawn, C. R., and Barth, T. J., "A Finite-Volume Euler Solver for Computing Rotary-Wing Aerodynamics on Unstructured Meshes," *Journal of the American Helicopter Society*, Vol. 38, No. 2, 1993, pp. 61–67.

[8]Hansen, M. O. L., Michelsen, J. A., and Sørensen, N. N., "Navier-Stokes Solver for Rotating Blade," European Wind Energy Conf., Oct. 1994.

[9]Baldwin, B. S., and Lomax, H., "Thin Layer Approximation and Algebraic Model for Separated Turbulent Flows," AIAA Paper 78-257, Jan. 1978.

[10]Spalart, P. R., and Allmaras, S. R., "A One-Equation Turbulence Model for Aerodynamic Flows," AIAA Paper 92-0439, Jan. 1992.

[11]Baldwin, B. S., and Barth, T. J., "A One-Equation Turbulence Transport Model for High Reynolds Number Wall-Bounded Flows," NASA TM 102847, Aug. 1990.

[12]Wu, J. C., "Theory of Aerodynamic Force and Moment in Viscous Flows," *AIAA Journal*, Vol. 19, No. 4, 1981, pp. 432–441.

[13]Harlow, F. H., and Welch, J. E., "Numerical Calculation of Time-Dependent Viscous Incompressible Flow with Free Surface," *Physics of Fluids*, Vol. 8, No. 12, 1965, pp. 2182–2189.

[14]Rosenfeld, M., Kwak, D., and Vinokur, M., "A Solution Method for the Unsteady Incompressible Navier-Stokes Equations in Generalized Coordinate Systems," AIAA Paper 88-0718, Jan. 1988.

[15]Chorin, A. J., "Numerical Solution of the Navier-Stokes Equations," *Mathematics of Computation*, Vol. 22, 1968, pp. 745–762.

[16]Kim, J., and Moin, P., "Application of a Fractional Time-Step Method to Incompressible Navier-Stokes Equations," *Journal of Computational Physics*, Vol. 59, 1985, pp. 308–323.

[17]Chorin, A. J., "A Numerical Method for Solving Incompressible Viscous Flow Problems," *Journal of Computational Physics*, Vol. 2, No. 1, 1967, pp. 12–26.

[18]Merkle, C. L., and Athavale, M., "Time-Accurate Unsteady Incompressible Flow Algorithm Based on Artificial Compressibility," AIAA Paper 87-1137, June 1987.

[19]Rogers, S. E., and Kwak, D., "An Upwind Difference Scheme for Time-Accurate Incompressible Navier-Stokes Equations," AIAA Paper 88-2883, June 1988.

[20]Rogers, S. E., Kwak, D., and Kiris, C., "Steady and Unsteady Solutions of the Incompressible Navier-Stokes Equations," *AIAA Journal*, Vol. 29, No. 4, 1991, pp. 603–610.

[21]Chakravarthy, S. R., "Relaxation Methods for Unfactored Implicit Upwind Schemes," AIAA Paper 84-0165, Jan. 1984.

[22]MacCormack, R. W., "Current Status of Numerical Solutions of the Navier-Stokes Equations," AIAA Paper 85-0032, Jan. 1985.

[23]Pulliam, T. H., "Artificial Dissipation Models for the Euler Equa-tions," *AIAA Journal*, Vol. 24, No. 12, 1986, pp. 1931–1940.

[24]Roe, P. L., "Approximate Riemann Solvers, Parameter Vectors, and Difference Schemes," *Journal of Computational Physics*, Vol. 43, No. 2, 1981, pp. 357–372.

[25]Srinivasan, G. R., Raghavan, V., Duque, E. P. N., and McCroskey, W. J., "Flowfield Analysis of Modern Rotors in Hover by Navier-Stokes Method," *Journal of the American Helicopter Society*, Vol. 38, No. 3, 1993, pp. 3–13.